

## Impact of beam coupling impedance on crab cavity noise induced emittance growth

N. Triantafyllou<sup>1,2</sup>, F. Antoniou,<sup>1</sup> H. Bartosik<sup>1</sup>, P. Baudrenghien<sup>1</sup>, X. Buffat<sup>1</sup>,  
R. Calaga<sup>1</sup>, Y. Papaphilippou<sup>1</sup>, T. Mastoridis<sup>3</sup>, and A. Wolski<sup>2</sup>

<sup>1</sup>CERN, Geneva, Switzerland

<sup>2</sup>University of Liverpool, Liverpool, United Kingdom

<sup>3</sup>California Polytechnic State University, San Luis Obispo, California, USA



(Received 6 November 2023; accepted 8 May 2024; published 8 July 2024)

Crab cavities will be deployed as a part of the High Luminosity Large Hadron Collider (HL-LHC) upgrade to mitigate the luminosity reduction induced by the crossing angle at the main experiments (ATLAS and CMS). Two prototype crab cavities have been installed in the CERN Super Proton Synchrotron (SPS) in 2018 for studies with proton beams. An issue of concern is the transverse emittance growth induced by noise in the crab cavity radio frequency (rf) system, which is anticipated to limit the performance of the HL-LHC. In measurements conducted in the SPS in 2018, the crab cavity noise-induced emittance growth was measured to be a factor of 4 lower than predicted from the existing analytical models. In this paper, it is shown that the observed discrepancy is explained by damping effects from the beam coupling impedance, which were not included in the models up to now. Using the van Kampen mode approach, a new theory is developed, suggesting that the impedance can separate the coherent tune from the incoherent spectrum leading to an effective reduction of the crab cavity rf noise-induced emittance growth. This mechanism is validated in tracking simulations using the SPS impedance model as well as in dedicated experimental measurements conducted in the SPS in 2022. The implications for the HL-LHC project are discussed.

DOI: [10.1103/PhysRevAccelBeams.27.071001](https://doi.org/10.1103/PhysRevAccelBeams.27.071001)

### I. INTRODUCTION

The aim of the High Luminosity Large Hadron Collider (HL-LHC) project [1,2] is to extend the LHC potential for discoveries by increasing the instantaneous (leveled) and integrated luminosity by factors of 5 and 10, respectively, beyond the current operational values. The crab cavities (CCs) are a key component of the upgrade, as they will be used to optimize the luminous region in the ATLAS [3] and CMS [4] detectors. In particular, they will restore the luminosity reduction caused by the large crossing angle, which is needed in order to mitigate long-range beam-beam effects. The CCs are radio frequency (rf) cavities that provide a transverse kick to the particles depending on their longitudinal position within the bunch, for restoring the head-on collisions at the interaction points [5].

Noise in the rf system of the CCs<sup>1</sup> is expected to result in undesired transverse emittance growth leading to a loss of luminosity [7]. The maximum allowed luminosity loss due to emittance growth driven by CC rf noise is set at 1% integrated over a physics fill, which translates to an emittance growth of 2%/h at the lowest  $\beta^*$  (0.15 m) reached at the end of the fill [8–10]. Given these very tight target values, a good understanding of the CC rf noise-induced emittance growth is critical for the HL-LHC performance.

To define the specifications for acceptable noise levels for the design of the HL-LHC CC rf system, a theoretical model was derived by Mastoridis and Baudrenghien (referred to as the “zero-coupling model” in what follows) to predict the transverse emittance growth caused by such noise [11]. This model was validated through numerical simulations with HEADTAIL [11]. To gain confidence in the model’s validity and its predictions for the HL-LHC, it was deemed necessary to benchmark it against experimental data.

<sup>1</sup>Past studies with CC rf noise performed in KEKB can be found in [6]. They were performed with leptons and with rf noise characterized by discrete spectral lines. Thus they are not applicable to the HL-LHC case, which entails proton beams (where the bunch length is a significant fraction of the rf wavelength) and broadband noise in the CCs.

Published by the American Physical Society under the terms of the *Creative Commons Attribution 4.0 International license*. Further distribution of this work must maintain attribution to the author(s) and the published article’s title, journal citation, and DOI.

Emittance growth measurements took place in the Super Proton Synchrotron (SPS at CERN), where two prototype CCs (which will be referred to as CC1 and CC2) of double quarter wave type [12], providing vertical deflection, were installed in 2018 for experimental tests with proton beams. The results from the first round of measurements did not agree with the predictions of the zero-coupling model as will be discussed in more detail in Sec. III of this paper. However, it was suspected that the beam coupling impedance, which is not included in the above-mentioned model, might have a significant effect on the transverse emittance growth. The main objective of this paper is to investigate the impact of the impedance on the CC rf noise-induced emittance growth in theory, in simulations, and in experiments.

This paper is structured as follows. Section II provides a recap of the standard approach (zero-coupling model) for predicting the emittance growth from CC rf noise. The results from the first campaign for the experimental benchmarking of this model that took place in 2018 are presented in Sec. III. A newly developed theory using the van Kampen mode approach, suggesting that the impedance can change the decoherence properties under the conditions of the experiment, is developed in Sec. IV. Section V presents results from tracking simulations, including the machine impedance, which supports the mechanism suggested by the newly developed theory and allows for quantitative comparison with experimental data. Section VI presents the experimental validation of the new theory with measurements that took place in 2022 in the SPS. The studies conclude with a discussion of the validity of the predictions of the zero-coupling model for the HL-LHC case in Sec. VII.

## II. THE ZERO-COUPLING MODEL

In the context of beam dynamics, the term noise concerns the deflecting field experienced by the beam. In the presence of CCs, it is considered that the CC voltage is of constant amplitude and with a phase adjusted so that the zero voltage is aligned with the longitudinal bunch core, therefore, kicking the bunch head and tail in opposite transverse directions. The deflecting voltage should ideally be strictly sinusoidal at the CC rf frequency. Yet it will suffer unwanted fluctuations coming from the low level rf, i.e., low power electronics, and the high level rf, e.g., power amplifier, cryogenic regulation. Typically, when discussing rf noise, phase fluctuations (resulting in misalignment of the deflecting field with the bunch core) and amplitude noise (pertaining to fluctuations of the deflecting voltage around the desired amplitude) are distinguished. Both cause unwanted fluctuations of the deflecting CC kick and result in transverse emittance growth in the plane of the kick, which can be predicted by the zero-coupling model [11]. Further details can be found in Sec. IV of [11].

The zero-coupling model predicts the transverse emittance growth due to CC noise assuming broadband rf noise

(discrete spectral lines are excluded). Furthermore, it is assumed that the rf amplitude and phase noise are uncorrelated that the CC phase is set such that the zero-crossing of the voltage coincides with the longitudinal bunch center and that there is no synchrotron radiation damping. These assumptions are valid for the case of the SPS in the studies presented in this paper.

According to the zero-coupling model, the emittance growth driven by CC rf noise is proportional to the noise power spectral density (PSD) summed over all betatron sidebands (phase noise) and synchrobetatron sidebands (amplitude noise) and can be computed using Eqs. (20) and (22) of [11]. The reason for the infinite sum is the aliasing of the rf noise spectrum, coming from the periodic passage of the beam over successive turns. For the experimental and the simulation studies presented in this paper, the noise spectra overlap and excite only the first vertical betatron (at  $\pm 7.8$  kHz) and synchrobetatron sidebands (at  $\pm 8.02$  and  $\pm 7.6$  kHz). The infinite sum, therefore, reduces to two terms (phase noise) and four terms (amplitude noise). As discrete spectral lines are excluded from this analysis, the rf noise spectrum can be considered as constant within the boundary of two synchrobetatron lines. Equations (20) and (22) of [11] can thus be simplified to

$$\frac{d\epsilon_y^{\text{geo}}}{dt} = 4\beta_{y,\text{CC}} \left( \frac{eV_{\text{CC}}f_{\text{rev}}}{2E_b} \right)^2 C_{\Delta A} (2\pi f_{\text{CC}}\sigma_t) S_{\Delta A}, \quad (1)$$

and

$$\frac{d\epsilon_y^{\text{geo}}}{dt} = 2\beta_{y,\text{CC}} \left( \frac{eV_{\text{CC}}f_{\text{rev}}}{2E_b} \right)^2 C_{\Delta\phi} (2\pi f_{\text{CC}}\sigma_t) S_{\Delta\phi}. \quad (2)$$

In the above formulas, the index  $y$  denotes the vertical plane,  $\epsilon_y^{\text{geo}}$  is the geometric emittance,  $\beta_{y,\text{CC}}$  is the beta function at the location of the CC,  $V_{\text{CC}}$  is the peak amplitude of the CC voltage,  $f_{\text{rev}}$  is the revolution frequency,  $E_b$  is the beam energy,  $e$  is the elementary charge, and  $\sigma_t$  is the rms bunch length in seconds. The parameters  $S_{\Delta A}$ ,  $S_{\Delta\phi}$  are the power spectral densities (PSDs) [13] of the noise at the excited first betatron and synchrobetatron (for the amplitude noise case) sidebands. The multiplication factors 4 and 2 show the contributions from two betatron (phase noise) and four synchrobetatron (amplitude noise) sidebands.  $C_{\Delta A}$  and  $C_{\Delta\phi}$  are correction factors to account for the bunch length; their definitions are given in [11]. Note that no collective force is considered in the above equations. The effect of a transverse damper (collective force proportional to, and in quadrature with transverse position averaged over the bunch) has been studied in [11], and formulas for the resulting reduction of emittance growth have been derived. However, the extension to a more general collective force (caused by machine

impedance) has not been studied in detail (transfer function  $H'[z]$  in Fig. 5 of [11]).

Amplitude and phase noise from the CC rf system are expected to result in emittance growth through decoherence [11,14,15]. If the noise spectrum overlaps with the sidebands of the betatron frequencies, it drives coherent betatron oscillations. In the presence of a betatron tune spread, which results in phase mixing of the particles within the bunch causing decoherence of the betatron oscillations, emittance growth is observed. The impact on bunch motion of amplitude noise in the CC rf system differs from that of phase noise. In the presence of amplitude noise, the head and the tail of the bunch are kicked in opposite directions resulting in intrabunch oscillations (related to head-tail mode 1).<sup>2</sup> In the presence of phase noise, the particles in the bunch receive kicks that are in phase, resulting in a shift of the bunch centroid that thus corresponds to dipole (or head-tail mode 0) motion.

### III. EXPERIMENTAL STUDIES IN 2018

The first round of measurements for the experimental benchmarking of the zero-coupling model took place in 2018, using the SPS in storage ring mode at 270 GeV, with four low-intensity bunches ( $3 \times 10^{10}$  p/b). Only CC2 was used, operating at 1 MV. The linear chromaticity was corrected to small positive values ( $Q'_x, Q'_y \sim 0.5$  units) in both transverse planes to minimize emittance growth from other sources [17]. The SPS octupoles were switched off; nevertheless, a residual nonlinearity was present in the machine coming mainly from multipole components in the dipole magnets [18,19]. The main parameters used for the emittance growth measurements in the SPS are listed in Table I.

To characterize the CC rf noise-induced transverse emittance growth, rf noise at a controlled level was injected into the CC rf system, and the emittance evolution was recorded for about 20–40 min. The injected noise was a mixture of amplitude and phase noise up to 10 kHz, overlapping and primarily exciting the first betatron and synchrotron sidebands. The phase noise was always dominant (i.e., much larger than the amplitude noise). For a meaningful comparison between the different levels of noise, the concept of effective phase noise is introduced: this is the phase noise level that, according to the zero-coupling model, would lead to the same emittance growth as that from both phase and amplitude noise. Emittance measurements using the SPS rotational wire scanners [20] were performed for five different levels of CC noise. The noise levels were measured with a signal source analyzer

<sup>2</sup>Here, the term head-tail modes refers to the azimuthal modes as defined in [16]. For the head-tail mode 0, the bunch moves transversely as a rigid unit. For the head-tail mode 1, the bunch also oscillates transversely but now the head and the tail of the bunch are 180° out of phase.

TABLE I. Parameter values in the experimental studies of emittance growth from CC rf noise, performed in the SPS in 2018.

Parameters	Values
Beam energy, $E_b$	270 GeV
Revolution frequency, $f_{\text{rev}}$	43.38 kHz
Bunch population, $N_b$	$3 \times 10^{10}$ particles
Horizontal/vertical betatron tune, $Q_x/Q_y$	26.13/26.18
Horizontal/vertical chromaticity, $Q'_x/Q'_y$	0.5/0.5
Vertical beta function at CC1, $\beta_{y,\text{CC1}}$	76.07 m
Vertical beta function at CC2, $\beta_{y,\text{CC2}}$	73.82 m
CC voltage, $V_{\text{CC}}$	1 MV
CC frequency, $f_{\text{CC}}$	400.8 MHz
Bunch length, $4\sigma_r$	1.7 ns
Initial horizontal normalized emittance, $\epsilon_x$	2 $\mu\text{m}$
Initial vertical normalized emittance, $\epsilon_y$	2 $\mu\text{m}$

E5052B [21] and are expressed as  $10 \log_{10} \mathcal{L}(f)$  (dBc/Hz). The “single-sideband phase noise”  $\mathcal{L}(f)$ , with  $f$  denoting the frequency, is the standard measure for characterizing instabilities in the frequency domain [22]. The power spectral densities in Eqs. (1) and (2) (following the IEEE conventions in [22]) are given by<sup>3</sup>  $S_{\Delta A, \Delta \phi}(f) = \mathcal{L}(f)$ , with  $S_{\Delta A}$  in 1/Hz and  $S_{\Delta \phi}$  in  $\text{rad}^2/\text{Hz}$ . A new beam was injected every time the transverse emittance reached very large values.

The emittance growth rates were obtained from a linear fit to the transverse emittance evolution for each noise setting. It should be noted that the normalized emittance,  $\epsilon_u = \beta_0 \gamma_0 \epsilon_u^{\text{geom}}$ , where  $\beta_0$  and  $\gamma_0$  are the relativistic factors, is used in the following. Even though emittance growth was observed mainly in the vertical plane, the total measured emittance growth, given by  $d\epsilon_y/dt + d\epsilon_x/dt$ , was considered in the analysis of the data from 2018 in order to account for betatron coupling effects [23].

The results of the measurements are summarized in Fig. 1, where the transverse emittance growth (blue) is plotted for different injected noise levels. A measurement without added noise in the CC yielded emittance growth rates of  $d\epsilon_x/dt = 0.6 \mu\text{m}/\text{h}$  and  $d\epsilon_y/dt = 0.44 \mu\text{m}/\text{h}$ . These values are subtracted from all the measurements that were made with controlled noise injected. The values predicted from the zero-coupling model [Eq. (2)] are also shown in Fig. 1: the calculations were performed using the parameter values given in Table I, and with the average bunch length over each observation window and the measured noise PSDs. The values of bunch length and power spectral density are listed in Table II. Although measurements were performed with four bunches in the

<sup>3</sup>The statistical signal processing definition of  $S(f)$  that includes both positive and negative frequencies [13] is used, while the IEEE standard [22] considers positive frequencies only, therefore, the factor of 2 difference.

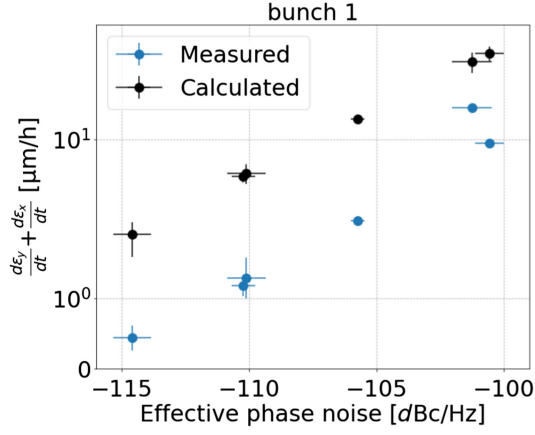


FIG. 1. Measured (blue) and theoretically calculated (black) using Eq. (2) transverse emittance growth rates as a function of the noise injected in the CC rf system during the experiments in the SPS in 2018. The theoretical values are calculated using the zero-coupling model.

ring, only the results for the first bunch are shown since the last three bunches were found to be longitudinally unstable [23].

It is evident that the zero-coupling model systematically overestimates the measured growth rates by a factor of 4 on average, over all noise settings (numerical values are listed in Table II). Simulations were performed to investigate various possible reasons for this discrepancy, including: beam losses, changes in the transverse distribution, variations of the longitudinal distribution [24], and the sensitivity to the nonlinearities of the SPS. However, none of these effects could explain the experimental observations. Furthermore, detailed studies excluded the possibility that the discrepancy is a result of some error in the analysis of the experimental data. Instead, it was suspected that the beam coupling impedance, which is not included in the zero-coupling model, can impact the CC rf noise-induced emittance growth and thus explain the experimental observations, as discussed in more detail in the following section.

TABLE II. Comparison between the measured and the calculated emittance growth rates for different noise levels (effective phase noise) in the SPS CC experiments in 2018. The average bunch length for each case is also given. The theoretical values are calculated using the zero-coupling model.

$10 \log_{10} \mathcal{L}(f)$ (dBc/Hz)	Growth rate ( $\mu\text{m/h}$ )		$\langle 4\sigma_t \rangle$ (ns)
	Measured	Calculated	
-114.8	0.47	1.83	1.67
-110.2	1.32	5.33	1.63
-110.1	1.18	5.29	1.75
-105.7	2.36	14.88	1.69
-101.3	18.08	40.04	1.72
-100.5	9.37	48.01	1.73

#### IV. ANALYTICAL MODEL INCLUDING IMPEDANCE EFFECTS

In order to understand how the impedance can impact the emittance growth driven by an external noise source, we follow the theoretical approach developed in [25], considering beam-beam interactions. However, here we shall rather consider a simpler collective force, which is characterized by a complex frequency shift. For simplicity, the development is limited to dipole noise, i.e., random kicks that affect identically all the particles in a bunch at a given turn. This corresponds to the CC phase noise, though neglecting the impact of the rf curvature. This aspect does not change qualitatively the mechanisms involved and is accurately taken into account in simulations (Sec. V).

##### A. Vlasov equation

We use the action-angle variables  $J$  and  $\theta$  relating to the transverse position  $x$  and momentum  $p_x$ :

$$x = \sqrt{2J} \cos(\theta), \quad (3)$$

$$p_x = -\sqrt{2J} \sin(\theta). \quad (4)$$

We assume that the initial beam distribution is uniform in angle and can, therefore, be written as

$$\Psi_0(J, \theta) = \frac{1}{2\pi} f_0(J), \quad (5)$$

where  $f_0$  is the initial distribution of actions. The effective Hamiltonian of the lattice  $H_0$  is that of an oscillator with amplitude detuning, and we define the betatron frequency:

$$\omega(J) \equiv \frac{\partial H_0}{\partial J}. \quad (6)$$

We add a collective force  $F_c$  proportional to the average position of the bunch  $\langle x \rangle$ :

$$F_c = -2\Delta\Omega_{\text{ext}} \langle x \rangle, \quad (7)$$

with  $\Delta\Omega_{\text{ext}}$  being the corresponding complex frequency shift. Thus we can write the Vlasov equation to the first order in a perturbation of the beam distribution  $\Psi_1$ :

$$\frac{\partial \Psi_1}{\partial t} + \frac{\partial \Psi_1}{\partial \theta} \omega(J) - \frac{\partial \Psi_0}{\partial J} \sqrt{2J} \sin(\theta) F_c = 0. \quad (8)$$

We will be looking for harmonic solutions of the form:

$$\Psi_1(J, \theta, t) = \frac{1}{2\pi} g(J) e^{i(\theta - \Omega t)}. \quad (9)$$

The Vlasov equation becomes an integral equation in the mode action distribution  $g(J)$  and the corresponding oscillation frequency  $\Omega$ :

$$(\Omega - \omega)g = -\frac{1}{2}\Delta\Omega_{\text{ext}}\frac{df_0}{dJ}\sqrt{2J}\int dJ\sqrt{2J}g. \quad (10)$$

### B. van Kampen modes

Following the van Kampen approach [26], we consider two sets of solutions to the Vlasov equation corresponding to a coherent mode  $g_c(J)$  and an incoherent spectrum  $g_k(J)$ .

Exploiting the freedom in the scale of the solution  $g_c(J)$ , we choose the corresponding mode frequency  $\Omega_c$  such that

$$\int dJ\sqrt{2J}g_c = 1. \quad (11)$$

The condition translates into the well-known dispersion relation [27]:

$$\int dJ\frac{J\frac{df_0}{dJ}}{\Omega_c - \omega} = -\frac{1}{\Delta\Omega_{\text{ext}}}. \quad (12)$$

This condition allows us to determine  $\Omega_c$  and write a solution of Eq. (10):

$$g_c = -\frac{1}{2}\Delta\Omega_{\text{ext}}\frac{\sqrt{2J}\frac{df_0}{dJ}}{\Omega_c - \omega}. \quad (13)$$

Following van Kampen [26], we find another set of solutions in the realm of distribution functions:

$$g_k = -\frac{1}{2}\Delta\Omega_{\text{ext}}\text{p.v.}\left(\frac{\sqrt{2J}\frac{df_0}{dJ}}{\Omega_k - \omega}\right) + \lambda_k\delta(J - k), \quad (14)$$

with  $k \in [0, \infty[$ . The notation p.v.( $\cdot$ ) indicates that an integration of the distribution function (e.g., to obtain statistical quantities) should be performed as a Cauchy principal value. For the coherent mode, the parameter  $\lambda_k$  in Eq. (14) is chosen such that

$$\int dJ\sqrt{2J}g_k = 1. \quad (15)$$

This condition yields

$$\lambda_k = \frac{1}{\sqrt{2k}}\left(1 + \Delta\Omega_{\text{ext}}\text{p.v.}\int dJ\frac{J\frac{df_0}{dJ}}{\Omega_k - \omega}\right). \quad (16)$$

By introducing this expression into the Vlasov equation, we determine the oscillation frequencies of the incoherent modes  $\Omega_k = \omega(k)$ .

A given perturbation can now be decomposed in terms of van Kampen modes characterized by the coefficients  $a_c$  and  $a_k$  for the coherent and incoherent part, respectively. The time evolution of the perturbation is then given by

$$\begin{aligned} \Psi_1(J, \theta, t) &= \frac{a_c}{2\pi}g_c(J)e^{i(\theta - \Omega_c)t} \\ &+ \int dk\frac{a_k}{2\pi}g_k(J)e^{i(\theta - \Omega_k)t}. \end{aligned} \quad (17)$$

### C. Decomposition of the initial kick

In order to obtain the coefficients, we introduce the scalar product

$$\langle g_n, g_m \rangle \equiv \int dJ\frac{g_n g_m^*}{\frac{df_0}{dJ}}. \quad (18)$$

It can be shown that the van Kampen modes are orthogonal. With the initial condition corresponding to a beam offset by  $\delta_{\text{ext}}$ , given by

$$\Psi_1(J, \theta, 0) = \delta_{\text{ext}}\sqrt{2J}\frac{d\Psi_0}{dJ}e^{i\theta}, \quad (19)$$

we apply the projection rule to obtain

$$a_c = \frac{\delta_{\text{ext}}}{|\langle g_c, g_c \rangle|}, \quad a_k = \frac{\delta_{\text{ext}}}{|\langle g_k, g_k \rangle|}. \quad (20)$$

The norms are given by

$$\langle g_c, g_c \rangle = \frac{1}{2}|\Delta\Omega_{\text{ext}}|^2 \int dJ\frac{J\frac{df_0}{dJ}}{|\Omega_c - \omega|^2}, \quad (21)$$

for the coherent mode and

$$\begin{aligned} \langle g_k, g_k \rangle &= \frac{1}{2k\frac{df_0}{dk}}\left(\pi^2\left|\frac{\Delta\Omega_{\text{ext}}}{\frac{\partial\omega}{\partial J}}\right|^2 k^2\left(\frac{df_0}{dk}\right)^2 + 2\pi k\frac{df_0}{dk}\frac{\Im\Delta\Omega_{\text{ext}}}{\left|\frac{\partial\omega}{\partial k}\right|}\right. \\ &\left. + \left|1 + \Delta\Omega_{\text{ext}}\text{p.v.}\int dJ\frac{J\frac{df_0}{dJ}}{\Omega_k - \omega}\right|^2\right), \end{aligned} \quad (22)$$

for the incoherent spectrum. A key step in the derivation of this expression is the use of the Poincaré-Bertrand formula to modify the order of integration, as in [28]. This leads to the first term (with a factor of  $\pi^2$ ) inside the parentheses. We note also that a single pole was assumed, imposing that  $\omega(J)$  is monotonic, but not necessarily linear at this point.

### D. Emittance growth

Computing the time evolution of the emittance by averaging Eq. (17), we find that it is constant, indicating that the emittance growth due to a kick is a second order

effect. Following [25], we obtain the second order term using Hamilton's equation for the action  $J$  and inserting it into the Vlasov equation:

$$\frac{dJ}{dt} = \frac{1}{\frac{\partial \Psi_0}{\partial J}} \left( \frac{\partial \Psi_1}{\partial t} + \frac{\partial \Psi_1}{\partial \theta} \omega(J) \right). \quad (23)$$

Averaging over  $J$  and realizing that, up to second order, the partial derivatives can be expressed as a total time derivative we obtain

$$\frac{d}{dt} \langle J \rangle_{\Psi_1(t)} = \frac{1}{2} \frac{d}{dt} \int dJ d\theta \frac{1}{\frac{\partial \Psi_0}{\partial J}} \Psi_1^2. \quad (24)$$

Using the expression for the time evolution of the distribution in terms of van Kampen modes [Eq. (17)], we obtain

$$\begin{aligned} \langle J \rangle_{\Psi_1(t)} &= \frac{\delta_{\text{ext}}^2}{8\pi^2} \int dJ d\theta \frac{1}{\frac{\partial \Psi_0}{\partial J}} \\ &\times \left( \frac{g_c(J) e^{i(\theta - \Omega_c t)}}{|\langle g_c, g_c \rangle|} + \int dk \frac{g_k(J) e^{i(\theta - \Omega_k t)}}{|\langle g_k, g_k \rangle|} \right)^2. \end{aligned} \quad (25)$$

As we are interested in the total emittance growth due to a single kick, we compute the limit of the average emittance toward infinite time. The limit exists if we assume that there exists a damping force, i.e.,  $\Im(\Omega_c) < 0.0$ :

$$\begin{aligned} \Delta \epsilon &\equiv \lim_{t \rightarrow \infty} \langle J \rangle_{\Psi_1(t)} - \epsilon_0^{\text{geo}} \\ &= \frac{1}{2} \delta_{\text{ext}}^2 \int \frac{dk}{|\langle g_k, g_k \rangle|}, \end{aligned} \quad (26)$$

where we have introduced the unperturbed rms emittance  $\langle J \rangle_{\Psi_0} \equiv \epsilon_0^{\text{geo}}$ . The contribution of the coherent mode  $a_c$  vanishes when considering the limit, showing that all the energy imparted to the collective motion is removed by the damping force and thus does not contribute to the emittance growth. Only the incoherent spectrum contributes to the emittance growth. This result is consistent with results obtained in the context of coherent beam-beam interactions [25]. In the absence of any collective force, the emittance growth due to a kick is given by  $\frac{1}{2} \delta_{\text{ext}}^2$  [29]; thus, it is convenient to define  $\eta$ , the emittance growth factor due to the collective force:

$$\eta \equiv \int \frac{dk}{|\langle g_k, g_k \rangle|}, \quad (27)$$

which can be solved numerically using the norm given by Eq. (22).

### 1. Gaussian distribution and linear detuning

We apply the results above to a practical configuration featuring linear detuning and a Gaussian distribution of the

particles. The Hamiltonian describing betatron motion of particles in the lattice is

$$H_0 = \int \omega(J) dJ, \quad (28)$$

where  $\omega(J)$  is the betatron frequency of a particle with amplitude  $J$ . In the case of linear detuning:

$$\omega(J) = (Q_0 + aJ)\omega_0, \quad (29)$$

where  $\omega_0$  is the revolution frequency,  $Q_0$  is the unperturbed tune, and  $a$  is the linear detuning coefficient. The unperturbed particle distribution is

$$f_0 = \frac{1}{\epsilon_0^{\text{geo}}} e^{-J/\epsilon_0^{\text{geo}}}. \quad (30)$$

Introducing the normalized action  $I \equiv J/\epsilon_0^{\text{geo}}$ , we have

$$\eta = \int dI \frac{I e^{-I}}{G(I)}, \quad (31)$$

with

$$\begin{aligned} G(I) &= \left| 1 + \frac{\Delta \Omega_{\text{ext}}}{a \omega_0 \epsilon_0^{\text{geo}}} (1 + I e^{-I} E_1(-I)) \right|^2 \\ &- 2\pi I e^{-I} \frac{\Im \Delta \Omega_{\text{ext}}}{|a \omega_0 \epsilon_0^{\text{geo}}|} + \pi^2 \left| \frac{\Delta \Omega_{\text{ext}}}{a \omega_0 \epsilon_0^{\text{geo}}} \right|^2 I^2 e^{-2I}. \end{aligned} \quad (32)$$

where  $E_1$  is the exponential integral. We find that the emittance growth factor is entirely determined by the external complex frequency shift scaled by the rms frequency spread  $\Delta \Omega_{\text{ext}}/(\omega_0 a \epsilon_0^{\text{geo}})$  or  $\Delta Q_{\text{ext}}/(a \epsilon_0^{\text{geo}})$ . This dependence is shown in Fig. 2. The presence of a damping component, represented by the imaginary part of  $\Omega_{\text{ext}}$ , reduces the emittance growth in all configurations. This behavior corresponds to the expectation for a classical

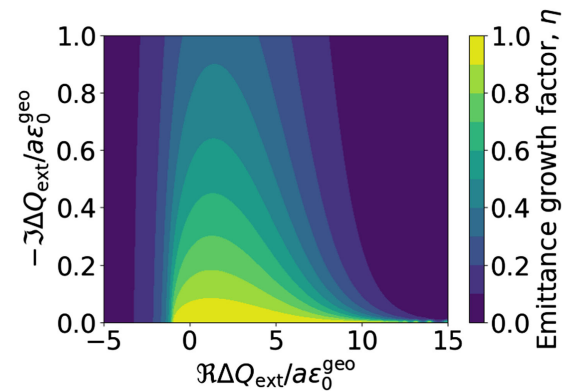


FIG. 2. Emittance growth factor with a positive detuning coefficient, as a function of the real and imaginary parts of the external frequency shift. The plot is produced using Eq. (31).

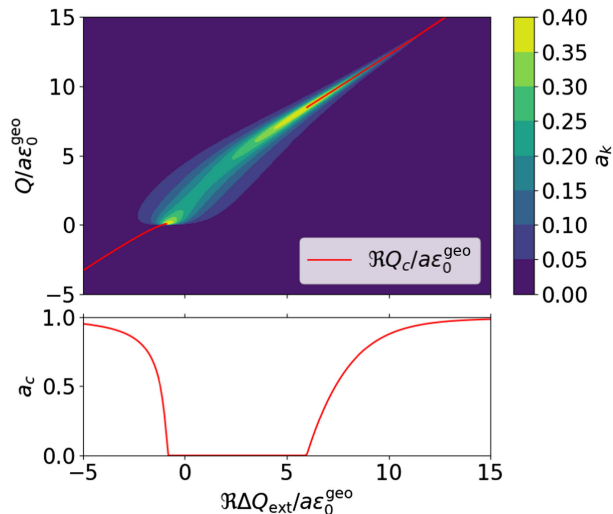


FIG. 3. Spectrum of oscillation resulting from a kick for different external frequency shifts  $\Re\Delta Q_{\text{ext}}$  (top plot). The imaginary part is kept constant at  $2 \times 10^{-4}$  and the detuning  $a\epsilon_0^{\text{geo}}$  is  $10^{-3}$ . The incoherent contribution is shown with a color scale, while the coherent mode is represented by a red line; the corresponding coherent mode coefficient  $a_c$  is shown on the bottom plot. The plot is produced using Eqs. (20)–(22).

resistive feedback. In addition, we observe that a real frequency shift can significantly reduce the emittance growth if the real frequency shift is much larger than the frequency spread. There is a strong asymmetry between negative and positive real frequency shifts. In this example, the detuning coefficient  $a$  is positive, in which case, a negative coherent frequency shift is favorable for suppression of the emittance growth. This can be understood with Fig. 3. The incoherent spectrum is mostly excited for positive real external frequency shifts, i.e., external frequency shifts matching the oscillation frequencies of individual particles. In this regime, Eq. (12) does not admit any solution for  $\Omega_c$ , implying that the coherent mode does not exist, and only incoherent modes are possible. Consequently, the collective force is inefficient at suppressing the emittance growth. On the contrary, for larger real external frequency shifts with either sign, the coherent mode dominates the dynamics and thus the emittance growth is efficiently suppressed by the collective force.

### E. Experimental validation with dipole noise

Using the same setup of the SPS as for the CC noise studies (Table I), a set of experiments were performed to measure the emittance growth rates resulting from an external noise source. In order to satisfy the assumption in the analytical model that there is a uniform kick over the length of the bunch, dipole noise was introduced using the transverse feedback kicker. The measured emittance growth compared to the model is shown in Fig. 4 for different levels of amplitude detuning controlled by the SPS Landau

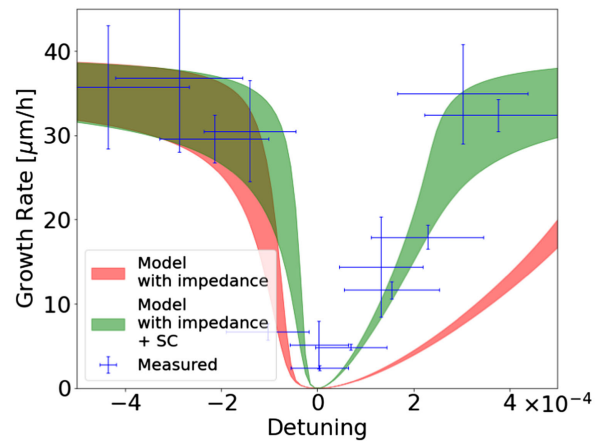


FIG. 4. Measured emittance growth rate (blue) while applying dipole noise to the beam in the SPS as a function of amplitude detuning obtained by varying the strength of the SPS Landau octupole magnets. The red and green shaded areas correspond to predictions from the analytical model, which includes the impedance effects for the condition of the experiments including uncertainties. The red curve is based on the complex tune shift driven by the impedance only. The green curve corresponds to the same model including a shift of the incoherent spectrum due to space charge (for details see text). The plot was produced using Eq. (31) as a multiplicative factor to the emittance growth rate expected from the dipole kick in the absence of impedance. The latter value was obtained from a fit on the measured data since the instrument applying the dipole noise to the beam was not calibrated.

octupoles. Each data point was obtained by injecting a beam, ramping the beam energy, and then injecting noise for up to 10 min while monitoring the transverse emittance with wire scanner measurements. The uncertainty in the detuning is dominated by the growth of the emittance during the measurement. For the configurations with a low detuning, the variation of the emittance is small and the uncertainty is dominated by the space-charge tune spread, corresponding to an rms tune spread of approximately  $6 \times 10^{-5}$ . This contribution is introduced as an uncertainty, since the detuning is not linear with the transverse action and varies with each particle's synchrotron motion. These features are not taken into account in the analytical model described above. The uncertainty on the measured growth rate is given by the linear fit of the emittance measurement as a function of time.

To obtain predictions from the theoretical model (red area), we define  $\Delta Q_{\text{ext}}$  based on the real tune shift and damping rate of mode 0 obtained with tracking simulations (PyHEADTAIL [30]) taking into account the full transverse impedance model of the SPS [31] ( $\Re\Delta Q \approx 6 \times 10^{-4}$ ,  $1/\tau \approx 1.6 \times 10^{-4}$ ). The shaded area represents an uncertainty of 50% on the damping rate, caused by the uncertainty on the measured chromaticity, and an uncertainty of 10% on the amplitude of the injected noise. The agreement of the model with the experimental data is rather

poor, while good agreement could be obtained by considering a rough model of the space-charge interaction. Indeed, the space-charge forces yield an additional shift of the incoherent spectrum with respect to the coherent mode, which we model by adding the tune shift caused by space charge ( $\Delta Q_{SC} \approx -3.7 \times 10^{-4}$ ) to  $\Delta Q_{ext}$ .

## V. SIMULATION STUDIES WITH CRAB CAVITY NOISE

In this section, we use tracking simulations to demonstrate the emittance growth suppression mechanism described in Sec. IV. The tracking simulations take into account the impact of the CC rf curvature and were performed for conditions as close as possible to those of the 2018 experiments with CC noise, in order to allow for easier comparison with the experimental results. Unless stated, otherwise, the parameter values used are those shown in Table I.

In the simulation setup, the SPS ring is modeled in two segments by linear transport maps. In between the linear transport maps, particles receive kicks from the lumped wakefields as obtained from the SPS impedance model [31], and kicks from the CC noise, respectively. The effect of the vertical CC rf amplitude noise is applied as

$$\Delta y'_j = \frac{eV_{CC}}{E_b} \Delta A_j \sin\left(\frac{2\pi f_{CC}}{c\beta_0} z_j\right), \quad (33)$$

and the CC rf phase noise is applied as

$$\Delta y'_j = \frac{eV_{CC}}{E_b} \Delta \phi_j \cos\left(\frac{2\pi f_{CC}}{c\beta_0} z_j\right), \quad (34)$$

where  $j$  denotes the turn number and  $y'$  and  $z$  are the vertical angles and longitudinal particle co-ordinates, respectively. The parameters  $\Delta A_j$  and  $\Delta \phi_j$  are random numbers taken from normal distributions with zero mean and standard deviations of  $\sigma_{\Delta A}$  and  $\sigma_{\Delta \phi}$ , respectively. For a white noise spectrum, the power spectral density of these noise kicks can be computed as

$$S_{\Delta A} = \frac{\sigma_{\Delta A}^2}{f_{rev}} \quad (35)$$

and

$$S_{\Delta \phi} = \frac{\sigma_{\Delta \phi}^2}{f_{rev}}. \quad (36)$$

In the simulations, the value of  $2.7 \times 10^{-3}$  is used for both  $\sigma_A$  and  $\sigma_\phi$ : this is stronger than the noise levels injected in the CC rf system in the 2018 experiments, but the larger value was used since it results in a reasonable emittance growth in the simulation time of  $10^5$  turns ( $\sim 2.5$  s in the SPS). Finally, detuning effects, such as detuning with

amplitude and chromaticity, are introduced as a change of the phase advance of the individual particles.

First, the emittance growth was simulated in the presence of phase and amplitude noise, with and without the SPS impedance model, for a range of vertical amplitude detuning coefficients,  $\alpha_{yy}$ . The horizontal detuning coefficient and the cross term were left at zero, i.e.,  $\alpha_{xx} = \alpha_{xy} = 0$ . The emittance growth rate was obtained from a linear fit to the normalized emittance values over the length of the simulation. For every  $\alpha_{yy}$  setting, 20 simulation runs were performed to reduce the uncertainty of the results. For each run, the initial bunch distribution and the sequence of the uncorrelated noise kicks were regenerated. For completeness, the emittance growth induced by a pure dipolar noise kick was also included in the simulations. The latter is applied as  $\Delta y'_j = \theta_j$ , where the values  $\theta_j$  correspond to the noise kick and are random numbers taken from a normal distribution with zero mean and standard deviation  $\sigma_\theta$ . For a white noise spectrum, the power spectral density of the kicks can be computed as  $S_\theta = \sigma_\theta^2 / f_{rev}$ .

Figure 5 illustrates the dependence of the simulated emittance growth rates on the amplitude detuning coefficient,  $\alpha_{yy}$ , normalized to the prediction of the zero-coupling model. The secondary horizontal axis shows the resulting rms tune spread, computed as  $\text{rms}(\Delta Q_y) = \alpha_{yy} \epsilon_y^{\text{geo}}$ . The predictions were obtained using Eqs. (1) and (2) for amplitude and phase noise, respectively, while for the dipole noise case Eq. (23) in [29] was used.

When the wakefields are not included in the simulations, the emittance growth rates that are obtained are in good agreement with the predictions of the zero-coupling model, except for  $\alpha_{yy} = 0$ . However, this is expected since the theory assumes the observation time to be long compared to the decoherence time, which is not valid for these simulation points.

When the wakefields are applied to the beam, there is a clear suppression of the emittance growth driven by dipolar and CC rf phase noise. This suppression depends on the detuning coefficient and is asymmetric between negative and positive values of the detuning coefficient. For the case of dipole noise, the analytical prediction from the new model developed in Sec. IV is also plotted. The small quantitative disagreement of the new theory with the simulation results could be explained by the fact that the simulations include the effect of the real wakefields over the longitudinal distribution of the bunch, whereas the theory assumes a damping force (resulting from the wakefields) which acts uniformly on the entire beam. For the CC rf phase noise case, over the realistic range of betatron tune spread values for the SPS experimental conditions (gray shaded area) the emittance growth suppression reaches a factor of 4 or 5. This is very close to the experimental observations of 2018 and the simulation results show a behavior similar to the one expected from the new theory

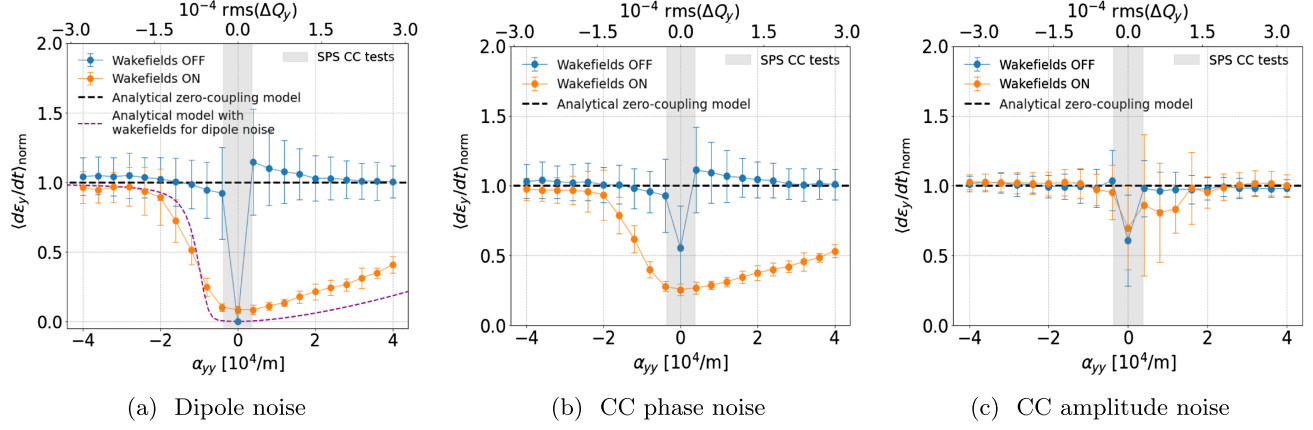


FIG. 5. Simulated vertical emittance growth driven by (a) dipolar noise, (b) CC rf phase noise, and (c) CC rf amplitude noise, with and without machine impedance, as a function of the vertical detuning coefficient,  $\alpha_{yy}$  (lower horizontal axis). The resulting rms tune spread,  $\text{rms}(\Delta Q_y) = \alpha_{yy} \epsilon_y^{\text{geo}}$ , is shown on the upper horizontal axis. The displayed emittance growth rates,  $\langle d\epsilon_y/dt \rangle_{\text{norm}}$ , are the average over 20 simulation runs and normalized with the corresponding predictions from the zero-coupling model computed with Eqs. (1) and (2). The gray shaded area indicates the estimated tune spread induced by residual nonlinearities of the SPS [18,19] and chromaticity ( $Q'_{x,y} = 0.5$ ).

presented in Sec. IV. Furthermore, Fig. 5 shows that the emittance growth driven by CC rf amplitude noise is not suppressed by impedance-induced effects. These observations are in agreement with the theory of Sec. IV, as the phase noise (which is similar to a dipolar noise kick but with a high-order distortion) is associated with head-tail mode 0, while the amplitude noise is associated with head-tail mode 1.

The sensitivity of the emittance growth suppression mechanism to the linear chromaticity, as an additional source of tune spread, was also investigated through simulation studies. The results are shown in Fig. 6. No negative chromaticity values were studied, as they would result in the head-tail mode 0 instability. Figure 6 shows that the impact of the linear chromaticity on the maximum emittance growth suppression (observed for  $\alpha_{yy} = 0$ ) is weak. In the regime of negative detuning coefficients, the increasing values of chromaticity enlarge the region of emittance growth suppression.

The next set of simulations aimed at validating that the mechanism behind the emittance growth suppression from the impedance is the separation of the coherent tune (head-tail mode 0) from the incoherent tune spectrum, as suggested in Sec. IV. Figure 7 illustrates the simulated emittance growth driven by CC rf phase noise when the SPS impedance is taken into account as a function of different values of coherent tune shift scaled by the incoherent tune spread. The simulations for this parametric study were actually performed for different values of the bunch intensity (upper horizontal axis), which translates to different values of coherent tune shift from the impedance. The incoherent spectrum was introduced through amplitude detuning, for  $\alpha_{yy} = 12000 \text{ m}^{-1}$ .

Three different regimes are visible in Fig. 7. For small (absolute) values of coherent tune shift,  $\lesssim 10^{-4}$ , the

emittance growth rates appear independent of the coherent tune shift value and in good agreement with the predictions of the zero-coupling model. For increasing coherent tune shift values, the emittance growth rates decrease and eventually saturate. The above-described dependence of the emittance growth suppression on the coherent tune shift is consistent with the mechanism suggested in Sec. IV: the emittance growth suppression is a result of the separation of

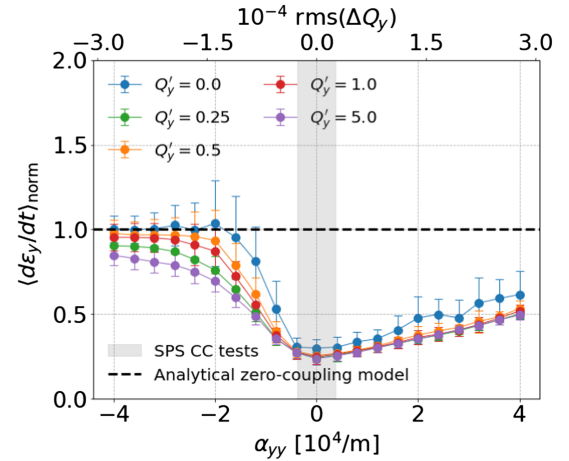


FIG. 6. Simulated vertical emittance growth driven by CC rf phase noise with impedance effects as a function of the vertical detuning coefficient,  $\alpha_{yy}$ . The resulting rms tune spread,  $\text{rms}(\Delta Q_y) = \alpha_{yy} \epsilon_y^{\text{geo}}$ , is shown on the upper horizontal axis. The simulation is performed for different values of linear chromaticity,  $Q'_y$ . The displayed emittance growth rates,  $\langle d\epsilon_y/dt \rangle_{\text{norm}}$ , are the average over the 20 simulation runs and normalized with the corresponding predictions from the zero-coupling model computed with Eq. (2). The gray shaded area indicates the estimated tune spread induced by residual nonlinearities of the SPS [18,19] and  $Q'_{x,y} = 0.5$ .

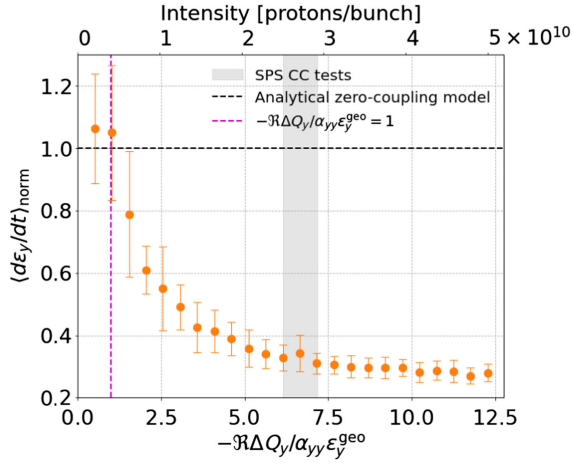


FIG. 7. Simulated vertical emittance growth driven by CC rf phase noise as a function of the negative coherent tune shift,  $-\Re\Delta Q_y$ , scaled by the rms incoherent tune spread,  $\alpha_{yy}\epsilon_y^{\text{geo}}$ . Machine impedance is included, and the change in incoherent tune spread results from a change in bunch intensity. The emittance growth rates,  $\langle d\epsilon_y/dt \rangle_{\text{norm}}$ , are the average over the 20 simulation runs and normalized with the corresponding predictions from the zero-coupling model computed with Eq. (2). The vertical magenta line shows the point, where the coherent tune shift is equal to the incoherent tune spread. The gray vertical band indicates the coherent tune shift expected for the experimental conditions of SPS CC tests in 2018.

the coherent mode from the incoherent spectrum, as the beam impedance leads to a shift of the coherent tune. This mechanism is also supported by Fig. 8, which shows the frequency spectra of the vertical bunch motion as obtained from Fourier analysis of the turn-by-turn motion of the bunch centroid for  $10^6$  turns (Schottky noise [32]). The frequency of the coherent mode (highest amplitude) is shown by a vertical magenta line. The simulations were performed following the same procedure as for the studies

presented above, but without applying the noise kicks on the bunch to minimize the external perturbations: this allows a clear tune spectrum to be obtained, resulting only from the wakefields and the detuning with amplitude.

By comparing Figs. 7 and 8, it becomes evident that there is no suppression of the emittance growth when the coherent tune lies inside the incoherent spectrum [Fig. 8(a)]. Once the coherent mode emerges from the incoherent spectrum [Fig. 8(b)], the emittance growth suppression mechanism becomes apparent. Eventually, when the coherent mode is well separated from the incoherent spectrum, the dependence on the bunch intensity saturates [Fig. 8(c)].

Finally, simulations were performed to characterize the effect of the CC rf curvature on the emittance growth suppression mechanism. To this end, emittance growth driven by CC rf phase noise was simulated over a range of different CC wavelengths, for a constant bunch length of  $4\sigma_t = 1.7$  ns, and for a vertical detuning coefficient of  $\alpha_{yy} = 12000 \text{ m}^{-1}$ . The results are summarized in Fig. 9, where the simulated growth rates, normalized to the predictions of the zero-coupling model, are shown as a function of the ratio between the bunch length and the CC wavelength.

Figure 9 illustrates, as expected, that the simulation results without the wakefields are in very good agreement with the predictions of zero-coupling model, within the error bars. In the presence of wakefields, the suppression of the emittance growth appears stronger for longer CC wavelengths. This could be explained by the fact that for wavelengths much longer than the bunch length, the bunch is affected mostly by the linear part of the CC kick, which is closer to a pure dipolar excitation. Indeed, for short bunches compared to the CC wavelengths, the simulated emittance growth agrees very well with the predictions of the new analytical model, developed in Sec. IV, which

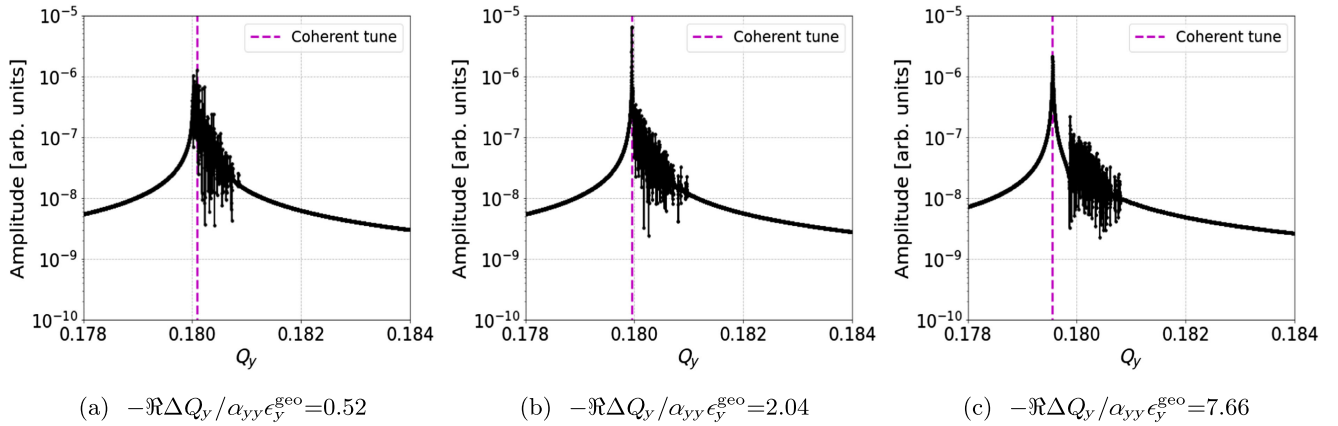


FIG. 8. Frequency spectra of the vertical bunch centroid motion in the presence of the SPS transverse impedance model, calculated over  $10^6$  turns with  $5 \times 10^4$  macroparticles for three different intensity values, and hence different shifts of the coherent tune (from the impedance) with respect to the nominal value of 0.18. The incoherent tune spread is introduced primarily through detuning with amplitude, with  $\alpha_{yy} = 12000 \text{ m}^{-1}$ .

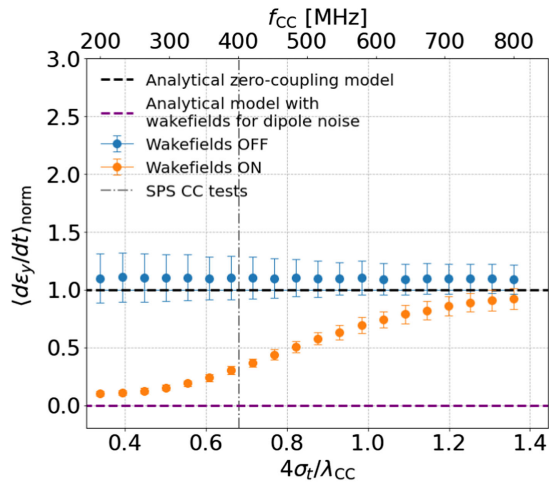


FIG. 9. Dependence of the simulated vertical emittance growth driven by CC rf phase noise on the ratio of the bunch length,  $4\sigma_t$ , and the CC wavelength,  $\lambda_{CC}$ . For the latter, the corresponding CC frequency  $f_{CC}$  is also shown (upper horizontal axis). The emittance growth rates,  $\langle d\epsilon_y/dt \rangle_{\text{norm}}$ , are the average over 20 simulation runs and normalized by the corresponding predictions from the zero-coupling model computed with Eq. (2). For reference, the magenta line represents the prediction of the new analytical model developed in Sec. IV, which is a horizontal line since the rf curvature of the CC phase noise is neglected. For the specific simulation conditions, a complete emittance growth suppression is predicted.

includes the impact of the impedance for a pure dipolar excitation (magenta dashed line). In particular, for the parameters of the study, the new model predicts that the emittance growth should be fully suppressed. For shorter wavelengths, the bunch is affected by the rf curvature of the CC, and the suppression mechanism becomes less effective and even disappears.

## VI. EXPERIMENTAL STUDIES IN 2022

The second experimental campaign with CCs in the SPS took place in 2022 with the aim to investigate effects of impedance and amplitude detuning on emittance growth from CC rf phase noise. It consisted of two sessions, in May and in September, with slightly different parameter values, which are listed in Table III. The displayed CC voltage and noise level values were measured during the experiments with the head-tail monitor [33,34] and a signal source analyzer [21], respectively. The bunch length values are the average measured bunch length during the measurements. The background emittance growth rates correspond to the measured emittance growth induced by other sources (without noise in CC1).<sup>4</sup> Generally, the measurements in 2022 were performed following the same

<sup>4</sup>The background emittance growth was measured in May 2022 with the octupoles turned off and in September 2022 with  $k_{\text{LOD}} = +30 \text{ m}^{-4}$ .

procedure as in 2018 and for very similar machine and beam conditions. There were, however, some differences, the main ones being that in 2022, the emittance growth measurements were conducted with CC1 rather than CC2 (due to difficulties that appeared in the calibration of CC2); slightly longer bunches were used in 2022 than in 2018; and in 2022 measurements were made using a single bunch in the machine, rather than four bunches. Furthermore, the small but nonzero linear transverse coupling observed in 2018 was corrected in 2022 using skew quadrupoles. In 2022 as in 2018, the noise injected into the CC rf system consisted of a mixture of phase and amplitude noise, overlapping the first betatron and synchrotron sidebands only, with the phase noise being dominant.

Different octupole settings were used, with the aim of reproducing the dependence of the emittance growth mechanism on the amplitude-dependent betatron tune shift, as already observed theoretically (Sec. IV) and in simulations (Sec. V). The octupole family consisting of the octupoles adjacent to the defocusing quadrupoles was used (LOD). For each setting of the octupoles, the evolution of the emittance was recorded over a period of about 20–30 min. Emittance measurements were made using a wire scanner, and the growth rate determined by a linear fit. For each setting of the octupoles, a freshly injected beam was used.

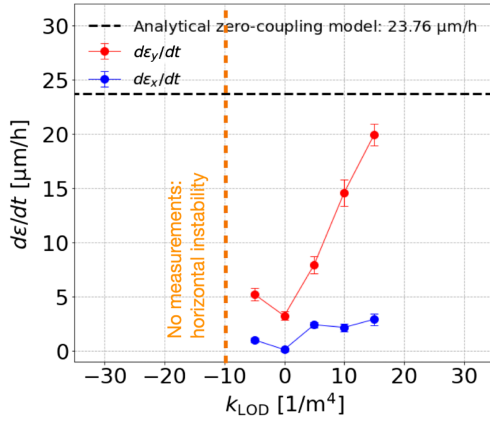
The experimental results from 2022 are summarized in Fig. 10 showing the measured horizontal and vertical emittance growth rates for different octupole strengths, after subtraction of the background emittance growth rate in the corresponding plane. Note that in the 2018 analysis, the total emittance growth rate given by  $d\epsilon_y/dt + d\epsilon_x/dt$  was considered, to account for coupling effects; in the 2022 measurements, however, the emittance growth in the horizontal plane is essentially independent of that in the vertical plane as the linear coupling was corrected. The predicted vertical emittance growth rate from the zero-coupling model (without including impedance effects) is also shown, as computed for the parameter values listed in Table III. The contribution from both amplitude and phase noise is taken into account.

In the first set of measurements, in May 2022, five octupole settings (of small or moderate strength) were tested. Figure 10(a) shows a clear dependence of the measured vertical emittance growth rate on the octupole strength and hence on the amplitude-dependent tune spread: the dependence is qualitatively very similar to that expected from the simulations. During this experiment, the emittance growth rate could not be measured for  $k_{\text{LOD}} = -10 \text{ m}^{-4}$  since the bunch was found to be horizontally unstable (resulting in loss of the beam). The most likely explanation for this instability is that the chromaticity was too low and may have drifted to small negative values causing a head-tail mode 0 instability.

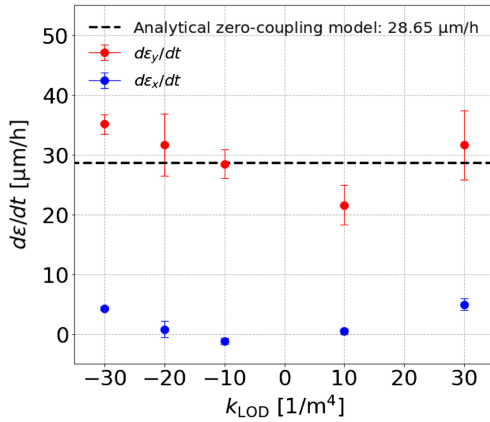
In the second set of measurements, in September 2022 [Fig. 10(b)], stronger octupole settings were used in order

TABLE III. Main parameters in the SPS CC emittance growth studies in 2022.

Parameters	May 2022	September 2022
Beam energy, $E_b$	270 GeV	270 GeV
Bunch population, $N_b$	$3 \times 10^{10}$ particles	$3 \times 10^{10}$ particles
Horizontal/vertical betatron tune, $Q_x/Q_y$	26.13/26.18	26.13/26.18
Chromaticity, $Q'_{x,y}$	$\sim 0.0-0.5$	$\sim 0.7$
Vertical beta function at CC1, $\beta_{y,CC1}$	76.07 m	76.07 m
CC1 voltage, $V_{CC1}$	1.1 MV	1.05 MV
CC1 frequency, $f_{CC1}$	400.8 MHz	400.8 MHz
Bunch length, $\langle 4\sigma_t \rangle$	1.83 ns	1.77 ns
Phase noise, $10 \log_{10} \mathcal{L}(f)$ at $f \approx 8$ kHz	-104.5 dBc/Hz	-103.3 dBc/Hz
Amplitude noise, $10 \log_{10} \mathcal{L}(f)$ at $f \approx 8$ kHz	-116.5 dBc/Hz	-123.3 dBc/Hz
Horizontal background emittance growth	0.81 $\mu\text{m}/\text{h}$	2.42 $\mu\text{m}/\text{h}$
Vertical background emittance growth	0.84 $\mu\text{m}/\text{h}$	1.72 $\mu\text{m}/\text{h}$



(a)



(b)

FIG. 10. Overview of the transverse emittance growth due to noise injected in the CC1 rf system for different octupole settings, as measured in (a) May 2022 and (b) September 2022. The predictions from the zero-coupling model, computed with Eqs. (1) and (2), are also shown (black dashed line). The error bars indicate the uncertainty of the linear fit on the emittance values acquired during each set of measurements.

to explore the regime where no suppression (from the machine impedance) of the emittance growth is expected and the growth rates predicted from the zero-coupling model should be restored. For this set of measurements, the linear chromaticity was increased to  $Q'_{x,y} = 0.7$  (to avoid the horizontal instability observed in May 2022). The experimental results of the vertical emittance growth appear to be in very good qualitative agreement with the PyHEADTAIL simulations including the machine impedance. Some quantitative discrepancies are observed and will be discussed further below. The measured vertical emittance growth rates also reproduce the asymmetry observed in the simulations for positive and negative octupole strengths. Note that the emittance growth in the horizontal plane is

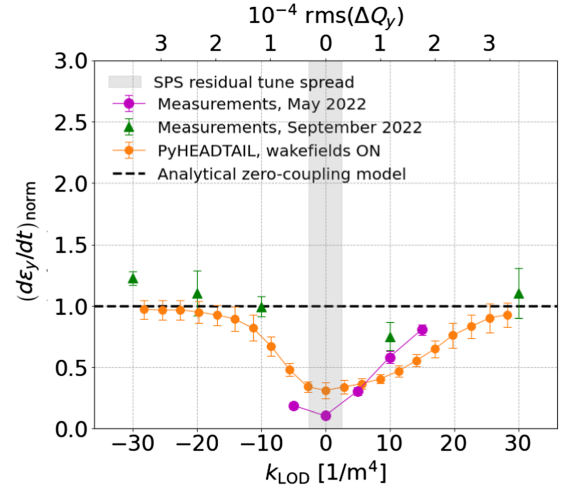


FIG. 11. Measured (magenta: May 2022 and green: September 2022) and simulated (orange) vertical emittance growth driven by phase noise injected in the CC rf system for different octupole settings. The displayed emittance growth rates are normalized with the corresponding predictions from the zero-coupling model computed with Eqs. (1) and (2). The error bars indicate the uncertainty of the linear fit on the measured emittance values during each set of measurements.

faster for larger octupole strength (in absolute value). A possible explanation, since the transverse coupling is minimized, could be the operation of the octupoles at very high currents. Further studies are needed to provide a conclusive explanation for the dependence of the horizontal emittance growth rate on the octupole strength, and the effect is considered to be beyond the scope of the current work.

A direct comparison of the measured vertical emittance growth rate with the simulation results from PyHEADTAIL including the SPS impedance model is shown in Fig. 11. The tracking simulations were performed with parameters very similar to the experimental conditions, as listed in Table III. The bunch length was set to  $4\sigma_t = 1.83$  ns, the linear chromaticity  $Q'_{x,y} = 0.5$ , and the CC1 voltage  $V_{CC1} = 1$  MV. The values of the vertical ( $\alpha_{yy}$ ) and cross-plane ( $\alpha_{xy}$ ) detuning coefficients were calculated using MAD-X [35] for each of the displayed  $k_{LOD}$  values, while the horizontal detuning coefficient  $\alpha_{xx}$  was left at zero. The rms tune spread (shown on the secondary horizontal axis) is computed taking into account both the  $\alpha_{yy}$  and  $\alpha_{xy}$  coefficients. The measured vertical emittance growth, after the subtraction of the background, is shown from both experiments that took place in the SPS in May 2022 (magenta) and September 2022 (green). Both measured and simulated emittance growth rates are normalized to the corresponding analytical prediction from the zero-coupling model. Note that, for the measured emittance growth rates, the computed analytical prediction includes the contribution from both amplitude and phase noise. In the simulations, only phase noise is considered.

Overall, the qualitative agreement between the experimental data and the simulations is very good. In particular, the measured vertical emittance growth rate clearly depends on the octupole strength and saturates for strong octupoles. In that case, the measured emittance growth rates are very close to the predictions of the zero-coupling model, providing confidence in its validity (under the appropriate conditions). Thus the experimental data from 2022 support the hypothesis that the beam impedance can result in suppression of the CC rf noise-induced emittance growth.

There is some uncertainty in the quantitative agreement: this is expected from the complex nature of the effects under investigation. Within the range of octupole strengths where the emittance growth suppression mechanism is effective, space charge may contribute to the differences between results from simulations and experiments. Space-charge effects have not yet been studied but could affect the emittance growth behavior by introducing additional betatron tune spread. Future simulation studies are planned to investigate this possibility, though it is computationally challenging. The level of quantitative agreement with the zero-coupling model in the regime of strong octupoles is very good, except for the case  $k_{LOD} = -30$  m<sup>-4</sup> where the measured vertical emittance growth appears about 25%

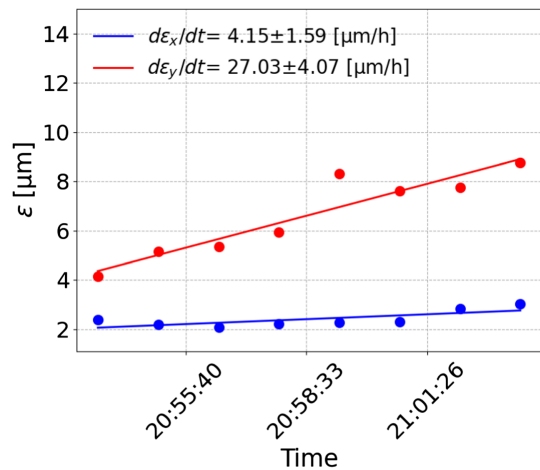


FIG. 12. Transverse emittance growth driven primarily by amplitude noise injected in the CC1 rf system, as measured in September 2022.

higher than predicted. However, this could be explained by a 10% uncertainty on the measurement of the CC1 voltage. An additional factor is the uncertainty of about  $\pm 0.5$  dB on the measurement of the rf noise power  $\mathcal{L}(f)$ , which translates to  $\pm 12\%$  in the estimated emittance growth rate.

#### A. Emittance growth driven by amplitude noise

Figure 12 shows the first experimental results of emittance growth in the SPS driven primarily by amplitude noise in the CC rf. The data were collected during the measurement campaign in September 2022, with the octupoles at  $k_{LOD} = -30$  m<sup>-4</sup>. The amplitude and phase noise in CC1 were measured to be  $-102$  and  $-122$  dBc/Hz, respectively, at  $\sim 8$  kHz. The emittance evolution for the above conditions is shown in Fig. 12.

The vertical emittance growth rate was about 25.41  $\mu\text{m}/\text{h}$  (after subtracting the background growth rate of  $de_y/dt = 1.62$   $\mu\text{m}/\text{h}$ , observed without noise injection). This is very close to the predictions of the zero-coupling model: 32.35 and 0.38  $\mu\text{m}/\text{h}$  from amplitude and phase noise, respectively (using the parameters in Table III). The measured emittance growth rate appears 20% lower than the predictions, however, this is within the uncertainty expected from the experimental setup. This agrees with the PyHEADTAIL simulations and with the theory introduced in Sec. V. However, the emittance growth due to amplitude noise for different values of amplitude detuning needs to be studied in future experimental campaigns.

## VII. CONCLUSIONS

During the SPS CC tests in 2018, it was found that the theoretical calculations of the vertical emittance growth rates from CC rf noise using the standard approach of the zero-coupling model overestimated the experimental results by a factor of 4 on average. A new theory based on

van Kampen modes was developed, which shows that this discrepancy can be explained by impedance-induced effects. In particular, when the coherent tune lies outside of the incoherent tune spectrum, part of the excitation from the external noise does not result in emittance growth. This effect was demonstrated in the SPS experimentally and is consistent with macroparticle tracking simulations. For sufficiently large values of betatron tune spread, i.e., when the coherent tune is inside the incoherent spectrum, the emittance growth rate predicted by the zero-coupling model is expected to be restored: this was also confirmed both experimentally and in tracking simulations.

The emittance growth suppression mechanism described in this paper is not expected to be observed for the conditions planned for the HL-LHC. Past studies for the LHC and HL-LHC, with complex bunch train structures and multiple interaction points with asymmetric phase advance, have shown that the coherent modes (dominated by the beam-beam interactions) are expected to lie inside the incoherent spectrum [36,37] and thus the zero-coupling model is applicable. The strategy for mitigating the emittance growth from CC rf noise in HL-LHC to meet the performance specifications of the machine is based on a feedback system that is under development [24,38]. An alternative solution would be to operate HL-LHC with slightly flat optics [39]: this would allow for smaller beta functions in the crabbing planes at the locations of the CCs (due to the higher beta function at the interaction points) and would thus reduce the emittance growth induced by CC rf noise.

### ACKNOWLEDGMENTS

We would like to thank L. R. Carver for his assistance in 2018 experimental campaign, as well as T. Levens and N. Bruchon for the help with the head-tail monitor and bunch length measurements, respectively. We would also like to thank J. Egli and N. Stapley who were in charge of the LLRF and controls in the SPS test-stand, during the machine development sessions. In addition, we are grateful to the SPS-OP for the preparation and operation of the machine development studies. We also thank E. Metral, R. Tomas, and N. Mounet for useful discussions on the transverse beam dynamics with crab cavities. This work was supported by the High Luminosity LHC project and partially by the U.S. Department of Energy, Office of Science, Office of High Energy Physics, under Award No. DE-SC-0019287.

---

[1] *CERN Yellow Reports: Monographs, vol. 10 (2020): High-Luminosity Large Hadron Collider (HL-LHC): Technical Design Report*, edited by I. Béjar Alonso, O. Brüning, P. Fessia, M. Lamont, L. Rossi, L. Taviani, and M. Zerlauth (2020), <https://doi.org/10.23731/CYRM-2020-0010>.

- [2] O. Brüning and L. Rossi, *The High-Luminosity Large Hadron Collider* (World Scientific, Singapore, 2015).
- [3] G. Aad *et al.* (ATLAS Collaboration), The ATLAS experiment at the CERN Large Hadron Collider, *J. Instrum.* **3**, S08003 (2008).
- [4] S. Chatrchyan *et al.* (CMS Collaboration), The CMS experiment at the CERN LHC, *J. Instrum.* **3**, S08004 (2008).
- [5] R. Calaga, Crab cavities for the high-luminosity LHC, in *Proceedings of the 18th International Conference on RF Superconductivity, Lanzhou, China* (JACoW, Geneva, Switzerland, 2018), THXA03.
- [6] K. Ohmi, R. Tomás, Y. Funakoshi, R. Calaga, T. Ieiri, Y. Morita, K. Nakanishi, K. Oide, Y. Ohnishi, Y. Sun, M. Tobiyama, and F. Zimmermann, Response of colliding beam-beam system to harmonic excitation due to crab-cavity rf phase modulation, *Phys. Rev. ST Accel. Beams* **14**, 111003 (2011).
- [7] L. Medina, R. Tomás, G. Arduini, and M. Napsuciale, Assessment of the performance of high-luminosity LHC operational scenarios: Integrated luminosity and effective pile-up density, *Can. J. Phys.* **97**, 498 (2019).
- [8] L. E. Medina Medrano, R. Tomas Garcia, G. Arduini, and M. Napsuciale, Effective pile-up density as a measure of the experimental data quality for high-luminosity LHC operational scenarios, CERN, Geneva, Technical Report No. CERN-ACC-2018-0003, 2018, <https://cds.cern.ch/record/2301928>.
- [9] P. Baudreghien and T. Mastoridis, Crab cavity rf noise: Update 2, in *Proceedings of the HL-LHC WP2/WP4 Meeting, Geneva, Switzerland* (2021), [https://indico.cern.ch/event/1044711/contributions/4389271/attachments/2264292/3861025/CC\\_Noise\\_Feedback\\_PB.pdf](https://indico.cern.ch/event/1044711/contributions/4389271/attachments/2264292/3861025/CC_Noise_Feedback_PB.pdf).
- [10] I. Efthymiopoulos, Luminosity estimates including noise from crab cavities (without feedback), in *Proceedings of the Special Joint HiLumi WP2/WP4/WP13 Meeting, Geneva, Switzerland* (2021), [https://indico.cern.ch/event/1044711/contributions/4389268/attachments/2264203/3844208/ie\\_WP2CCemitBU\\_14.06.2021.pdf](https://indico.cern.ch/event/1044711/contributions/4389268/attachments/2264203/3844208/ie_WP2CCemitBU_14.06.2021.pdf).
- [11] P. Baudreghien and T. Mastoridis, Transverse emittance growth due to rf noise in the high-luminosity LHC crab cavities, *Phys. Rev. ST Accel. Beams* **18**, 101001 (2015).
- [12] S. Verdú-Andrés, J. Skaritka, Q. Wu, B. P. Xiao, S. Belomestnykh, I. Ben-Zv, L. Alberty, K. Artoos, R. Calaga, O. Capatina, T. Capelli, F. Carra, R. Leuxe, N. Kuder, C. Zanoni, Z. Li, and A. Ratti, Design and prototyping of HL-LHC double quarter wave crab cavities for SPS test in *Proceedings of the 6th International Particle Accelerator Conference, Richmond, VA* (JACoW, Geneva, Switzerland, 2015), MOBD2.
- [13] A. Papoulis and S. U. Pillai, *Probability, Random Variables, and Stochastic Processes*, 4th ed. (McGraw Hill, Boston, 2002).
- [14] V. Lebedev, V. V. Parkhomchuk, V. D. Shiltsev, and G. Stupakov, Emittance growth due to noise and its suppression with the feedback system in large hadron colliders, *Part. Accel.* **44**, 147 (1993), <https://inspirehep.net/literature/1670149>.

- [15] V. Lebedev, Computer simulation of the emittance growth due to noise in large hadron colliders, Part. Accel. **44**, 165 (1993), <https://cds.cern.ch/record/248622>.
- [16] A. W. Chao, *Physics of Collective Beam Instabilities in High Energy Accelerators* (Wiley, New York, NY, 1993).
- [17] F. Antoniou, A. Alekou, H. Bartosik, T. Bohl, R. Calaga, L. Carver, J. Repond, and G. Vandoni, Emittance growth in coast in the SPS at CERN, *J. Phys. Conf. Ser.* **1067**, 022008 (2018).
- [18] M. Carlà, H. Bartosik, M. Beck, K. Li, and M. Schenk, Studies of a new optics with intermediate transition energy as alternative for high intensity LHC beams in the CERN SPS, in *Proceedings of the 9th International Particle Accelerator Conference IPAC'18, Vancouver, BC, Canada* (JACoW, Geneva, Switzerland, 2018), pp. 713–716.
- [19] A. Alekou, R. Appleby, H. Bartosik, R. Calaga, M. Carlà, and Y. Papaphilippou, SPS long term stability studies in the presence of crab cavities and high order multipoles, in *Proceedings of the 61st ICFA Advanced Beam Dynamics Workshop HB-2018, Daejeon, Korea* (JACoW, Geneva, Switzerland, 2018), pp. 284–286, [10.18429/JACoW-HB2018-WEP2PO008](https://doi.org/10.18429/JACoW-HB2018-WEP2PO008).
- [20] J. Bosser, J. Camas, L. Evans, G. Ferioli, R. Hopkins, J. Mann, and O. Olsen, Transverse emittance measurement with a rapid wire scanner at the CERN SPS, *Nucl. Instrum. Methods Phys. Res., Sect. A* **235**, 475 (1985).
- [21] K. Gheen, *Phase Noise Measurement Methods and Techniques* (Agilent Technologies, 2012), <https://studylib.net/doc/18034081/phase-noise-measurements>.
- [22] IEEE standard definitions of physical quantities for fundamental frequency and time metrology—random instabilities, *IEEE Std Std 1139-2008* (IEEE, New York, 2009), p. c1-35, [10.1109/IEEESTD.2008.4797525](https://doi.org/10.1109/IEEESTD.2008.4797525).
- [23] N. Triantafyllou, F. Antoniou, H. Bartosik, P. Baudrenghien, X. Buffat, R. Calaga, L. Carver, T. Mastoridis, Y. Papaphilippou, and A. Wolski, Investigation of damping effects of the crab cavity noise induced emittance growth, in *Proceedings of the 12th International Particle Accelerator Conference, IPAC-2021, Campinas, SP, Brazil* (JACoW, Geneva, Switzerland, 2021), pp. 2054–2057, [10.18429/JACoW-IPAC2021-TUPAB256](https://doi.org/10.18429/JACoW-IPAC2021-TUPAB256).
- [24] T. Mastoridis and P. Baudrenghien, Transverse emittance growth due to rf noise in crab cavities: Theory, measurements, cure, and high luminosity LHC estimates (to be published).
- [25] Y. Alexahin, A study of the coherent beam–beam effect in the framework of the Vlasov perturbation theory, *Nucl. Instrum. Methods Phys. Res., Sect. A* **480**, 253 (2002).
- [26] N. Van Kampen, On the theory of stationary waves in plasmas, *Physica (Amsterdam)* **21**, 949 (1955).
- [27] J.S. Berg and F. Ruggiero, Landau damping with two-dimensional betatron tune spread, CERN, Geneva, Technical Report, No. CERN-SL-96-071-AP, 1996, <https://cds.cern.ch/record/318826>.
- [28] N.I. Muskhelishvili, *Singular Integral Equations* (Wolters-Noordhoff Publishing, Groningen, Netherlands, 1958), p. 57.
- [29] D. Möhl, Sources of emittance growth, in *Proceedings of the CAS-CERN Accelerator School: Intermediate Accelerator Physics* (CERN, Geneva, Switzerland, 2006), p. 245, <https://cds.cern.ch/record/941314>.
- [30] PyHEADTAIL code repository, <https://github.com/PyCOMPLETE/>.
- [31] Repository of SPS impedance model, [https://gitlab.cern.ch/IRIS/SPS\\_IW\\_model](https://gitlab.cern.ch/IRIS/SPS_IW_model).
- [32] F. Caspers, Schottky signals for longitudinal and transverse bunched-beam diagnostics, in *Proceedings of the CAS-CERN Accelerator School: Intermediate Accelerator Physics* (2009), [10.5170/CERN-2009-005.407](https://doi.org/10.5170/CERN-2009-005.407).
- [33] R. Calaga, A. Alekou, F. Antoniou, R. Appleby, L. Arnaudon, K. Artoos, G. Arduini, V. Baglin, S. Barriere, H. Bartosik, P. Baudrenghien, I. Ben-Zvi, T. Bohl, A. Boucherie, O. Brüning, K. Brodzinski, A. Butterworth, G. Burt, O. Capatina, and A. Zwoznik, First demonstration of the use of crab cavities on hadron beams, *Phys. Rev. Accel. Beams* **24**, 062001 (2021).
- [34] T. E. Levens, K. Łasocha, T. Lefevre, M. Gašior, R. Jones, T. Włostowski, J. P. Ellis, and R. J. Steinhagen, Automatic detection of transverse beam instabilities in the large hadron collider, *Phys. Rev. Accel. Beams* **22**, 112803 (2019).
- [35] L. Deniau, MAD-X: Methodical Accelerator Design, <https://mad.web.cern.ch/madx/f>.
- [36] T. Pieloni, A study of beam-beam effects in hadron colliders with a large number of bunches, Ph.D. thesis, Ecole Polytechnique, Lausanne, 2008.
- [37] X. Buffat, W. Herr, T. Pieloni, and D. Valuch, Modeling of the emittance growth due to decoherence in collision at the Large Hadron Collider, *Phys. Rev. Accel. Beams* **23**, 021002 (2020).
- [38] P. Baudrenghien, T. Mastoridis, and B. N. Miller, Crab cavity rf noise feedback and transverse damper interaction, CERN, Report No. CERN-ACC-NOTE-2019-0006, 2019.
- [39] E. Metral, Run 4 operational scenario and status of optics v1.6, in *Proceedings of the 12th HL-LHC Collaboration Meeting, Uppsala, Sweden* (2022), [https://indico.cern.ch/event/1197424/contributions/5035904/attachments/2507124/4308131/HLLHCCollaborationMeeting\\_Uppsala\\_19-09-2022\\_EM.pdf](https://indico.cern.ch/event/1197424/contributions/5035904/attachments/2507124/4308131/HLLHCCollaborationMeeting_Uppsala_19-09-2022_EM.pdf).